Original scientific paper

https://doi.org/10.33180/InfMIDEM2026.203

Informacije MIDEM
Journal of Microelectronics, Electronic Components and Materials
Vol. 56, No. 2(2026), XX – XX

Structural Design and Simulation Analysis of a Single Proof Mass Triaxial Capacitive Accelerometer Based on Dual Staggered Seesaws

Weiwei Cao[1], Jianqiang Han[1, 2, *], Ge Shi[1], Shilong Zhao[1], Jiarui Liu[1]

[1]The College of Mechanical and Electrical Engineering, China Jiliang University, Hangzhou, 310018, China
[2]State Key Laboratory of Transducer Technology, shanghai, 200050, P.R.China

Abstract: Driven by the demand for high-sensitivity, low-noise, low-power capacitive accelerometers in geological hazard detection, vibration monitoring and other application scenarios, this paper presents a novel triaxial capacitive accelerometer. Four equal-height comb capacitors with unequal gaps are symmetrically arranged around the proof mass to sense the in-plane X- and Y-axis acceleration. Two staggered seesaw structures are integrated into the proof mass. Four comb capacitors of uneven height with identical gaps are arranged at each end of every seesaw to detect Z-axis acceleration. Its fabrication process is compatible with that of in-plane comb capacitors, eliminating the temperature sensitivity and fabrication complexity inherent in conventional sidewall capacitors. Theoretical calculations and finite element simulations show that the relative capacitance change ($\Delta C/C_0$) reaches 15.8% for in-plane motion and 9.0% for out-of-plane motion under 2 g acceleration, while cross-axis sensitivity is less than 3%. The theoretical Brownian noise densities are $1.37\mu g/\sqrt{Hz}$ for the X- and Y-axes, and $1.82\mu g/\sqrt{Hz}$ for Z-axis. These results demonstrate that the proposed accelerometer enables simultaneous detection of in-plane and out-of-plane accelerations with high sensitivity and low cross-axis interference.

Keywords: MEMS; triaxial capacitive accelerometer; dual staggered seesaws; comb capacitors

Konstrukcijsko načrtovanje in simulacijska analiza enokomponentnega triosnega kapacitivnega merilnika pospeška z eno preskusno maso, ki temelji na dvojnih zamaknjenih nihalih

Izvleček: Zaradi povpraševanja po visoko občutljivih, nizkošumnih in energetsko varčnih kapacitivnih merilnikih pospeška za odkrivanje geoloških nevarnosti, spremljanje vibracij in druge scenarije uporabe, članek predstavlja nov triosni kapacitivni merilnik pospeška. Štirje grebenasti kondenzatorji enake višine z neenakimi razmaki so simetrično razporejeni okoli preskusne mase za zaznavanje pospeška v ravnini osi X in Y. V preskusno maso sta vgrajeni dve premaknjeni nihalni strukturi. Na vsakem koncu nihalne strukture so razporejeni štirje grebenasti kondenzatorji neenake višine z enakimi razmaki za zaznavanje pospeška po osi Z. Njegov proizvodni postopek je združljiv s postopkom izdelave grebenastih kondenzatorjev v ravnini, kar odpravlja temperaturno občutljivost in zapletenost izdelave, značilni za konvencionalne stranske kondenzatorje. Teoretični izračuni in simulacije s končnimi elementi kažejo, da relativna sprememba kapacitivnosti ($\Delta C/C_0$) pri pospešku 2 g doseže 15,8% za gibanje v ravnini in 9,0% za gibanje izven ravnine, medtem ko je občutljivost med osmi manjša od 3%. Teoretične gostote Brownovega šuma znašajo 1,37 μg/√Hz za osi X in Y ter 1,82 μg/√Hz za os Z. Ti rezultati kažejo, da predlagani merilnik pospeška omogoča sočasno zaznavanje pospeškov v ravnini in izven ravnine z visoko občutljivostjo in nizkimi motnjami med osmi.

Ključne besede: MEMS; triosni kapacitivni merilnik pospeška; dvojni zamaknjeni vzmetni mehanizmi; grebenasti kondenzatorji

* Corresponding Author's e-mail: hjqsmx@sina.com.

1 Introduction

Low-range, low-noise, and low-power triaxial capacitive accelerometers are in high demand for geological hazard monitoring, vibration measurement, industrial automatic control, and large-scale structural health monitoring [1]-[3]. These devices commonly adopt equal-height comb capacitors for in-plane (X- and Y-axis) acceleration detection, where movable and fixed comb fingers share the same height as the proof mass. Under in-plane acceleration, the movable comb fingers attached to the proof mass move synchronously, changing the gap between adjacent fingers and thus modulating the capacitance. The in-plane acceleration can be determined by detecting such capacitance variations [4]-[6]. Comb-type accelerometers fabricated by surface micromachining show excellent compatibility with standard integrated circuit (IC) processes, enabling monolithic integration with capacitive readout circuits. By applying silicon-on-insulator (SOI) [7]-[9] or silicon-on-glass (SOG) [10], [11] technologies, the thickness of the proof mass and height of the comb capacitors can reach tens of micrometres, which effectively suppresses thermomechanical noise.

In contrast, out-of-plane (Z-axis) acceleration sensing remains a critical challenge. The first Z-axis sensing unit adopts gap-modulated parallel-plate capacitors and falls into two structural subtypes. In the first configuration, parallel-plate capacitors are fixedly bonded to a vertically translatable proof mass. Subjected to Z-axis acceleration, the proof mass moves axially and modulates capacitance by varying the electrode gap [12]-[15]. For the second variant, movable electrodes are fabricated on the bottom surface of a torsion-suspended proof mass, whereas fixed electrodes are patterned atop the underlying substrate. Z-axis acceleration triggers torsional deflection of the proof mass and consequent gap variation to realize signal acquisition [16], [17]. Both structures are predominantly fabricated by bulk micromachining; the proof mass is defined across the full thickness of the silicon wafer to deliver low thermomechanical noise. However, multi-step wafer bonding is required in fabrication, which increases the difficulty of monolithic integration.

The second Z-axis sensing unit employs unequal-height comb capacitors attached to a linearly translating proof mass. It works based on acceleration-induced changes in the overlapping area of comb fingers, yet this structure suffers from low Z-axis sensitivity. As an example, the Z-axis sensitivity of the accelerometer reported by Xie et al. is merely 1/16 of its in-plane counterpart [18]. Hamaguchi tried to match in-plane and out-of-plane sensitivity, but the optimization sacrificed in-plane performance, whose sensitivity drops to less than 1% of Xie's result [19].

The third type adopts sidewall capacitors integrated alongside both sides of the torsional suspended proof mass. Z-axis acceleration is detected via variations in the overlapping area of sidewall electrodes [20], [21]. Sidewall capacitors consist of stacked multilayer metal and dielectric films. Electrodes with different metal-layer thicknesses are arranged alternately on two sides of the torsional structure to realize differential capacitive readout. Sidewall-capacitor accelerometers suffer from two major insufficiencies.

First, the devices exhibit severe temperature drift owing to mismatched thermal expansion coefficients between metal and dielectric films. Experimental results from Qu et al. show that the measured structural temperature coefficients of sensitivity are 304 ppm/°C for in-plane axes and 800 ppm/°C for the out-of-plane axis, while the overall system temperature drift including circuit contribution reaches approximately 2850 [22]-[24] .

Second, the fabrication workflow features exceptional complexity, demanding sequential cyclic thin-film deposition and tight thickness control for every metal and dielectric layer [25], [26].

To overcome the aforementioned drawbacks, this paper presents a single-proof-mass triaxial capacitive accelerometer based on dual staggered seesaw structures. Unequal-height comb capacitors with identical initial gaps, arranged on both sides of two staggered seesaws embedded inside the proof mass, are utilized for Z-axis acceleration measurement. Torsional beams mechanically isolate the seesaw assemblies from the central proof mass and effectively restrain cross-axis coupling between in-plane and out-of-plane directions. The fabrication process of the proposed device is fully compatible with standard in-plane comb-capacitor technology, avoiding the inherent large temperature drift and intricate fabrication of conventional sidewall capacitors.

The present paper is organized as follows. Section 2 introduces the structural configuration and geometric parameters of the proposed accelerometer. Section 3 derives its stiffness, resonant frequency and Brownian noise density. Section 4 analyzes its in-plane and out-of-plane detection sensitivities. Section 5 evaluates its cross-axis sensitivity. Section 6 conducts modal and harmonic-response analyses. Section 7 describes the corresponding fabrication process. Finally, Section 8 summarizes the main conclusions.

2 The Structure of Triaxial Capacitive Accelerometers

Figure 1 depicts the structure of the proposed accelerometer. A proof mass is supported on the silicon substrate by eight serpentine beams. Comb capacitors C_{x1} and C_{x2} at the top and bottom sides of the proof mass are used for X-axis acceleration detection, while C_{y1} and C_{y2} on the left and right sides detect Y-axis acceleration. Each comb capacitor is structured with 48 pairs of comb fingers of identical height. A movable finger is spaced from its two neighbouring fixed fingers by distinct gaps d_1 and d_2, where d_2 equals four times d_1.

Two staggered seesaw structures are embedded within the proof mass. Each staggered seesaw structure with saw-tooth comb fingers is mechanically decoupled from the main proof mass for in-plane acceleration sensing by a pair of torsional tether beams, and the two pairs of beams jointly constitute the complete tether-beam connection network. Four sets of comb capacitors denoted C_{z1}, C_{z2}, C_{z3} and C_{z4} are arranged on both sides of these seesaws to sense Z-axis acceleration. Every set is formed by 20 pairs of comb fingers differing in height, with an identical gap d_1 separating movable and fixed electrodes. The structural parameters are summarized in Table 1.

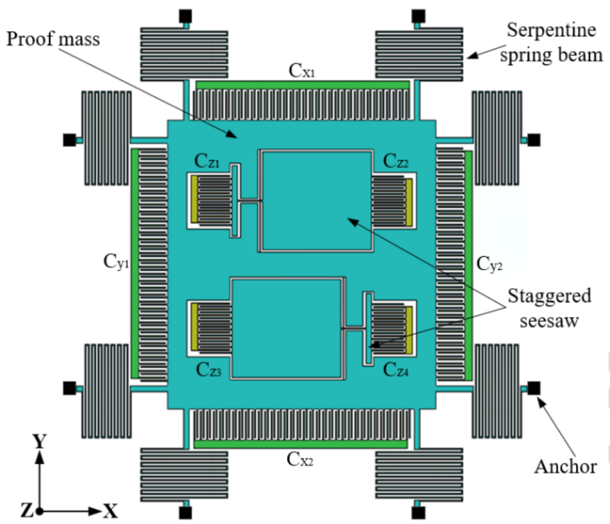

Figure 1: Schematic diagram of a triaxial capacitive accelerometer based on two staggered seesaws.

Table 1: Parameters and their values.

Parameter	Symbol	Value
Thickness of the proof mass	H	50µm
Narrow gap of fingers	d_1	4.5µm
Wider gap of fingers	d_2	18µm
Height of lower fingers	h_1	25µm
Height of higher fingers	h_2	50µm
Length of span beams	b	800µm
Length of tail beams	lt	400µm
Length of connecting beams	lc	40µm
Length of X- and Y-axes fingers	Lsx, Lsy	250µm
Length of Z-axis fingers	Lsz	300µm
Mass of movable structure	m	756µg

3 Static and Dynamic Performance of the Accelerometer

3.1 The Stiffness Coefficient of Elastic Beams

The serpentine elastic beam supports the proof mass on the substrate. As shown in Figure 2, beams ①-⑥ form a serpentine beam with 2 folded segments. Here, l_c, w, b, l_t, and H denote the length of the connecting beam, the width of each folded beam, the length of the span beam, the length of the tail beam, and the beam thickness. n represents the folding number of the serpentine beam.

The elastic coefficients along the three axes of the serpentine spring beam are calculated via Equations (1)-(3). These formulas are standard simplified engineering formulas directly provided in Fedder's analytical stiffness model for serpentine flexures [27], valid for the number of folded segments 4 ≤ n ≤ 20. With n = 15 in the proposed design, the stiffness calculation falls well within the applicable range, ensuring reliable results.

$$k_{\parallel} = \frac{48EI_{z,b}}{a^2(\tilde{a}+b)n^3} \tag{1}$$

$$k_{\perp} = \frac{48EI_{z,b}}{b^2(3\tilde{a}+b)n} \tag{2}$$

$$k_m = \frac{48GJ_b}{a^2((GJ_b/EI_{x,a})a+b)n^3} \tag{3}$$

Where J_b denotes the mass moment of inertia of the span beam, and G is the shear modulus of the material. $\tilde{a}$ is the moment of inertia and geometric correlation coefficient, without unit and the calculation formula is $\tilde{a}=I_{z,b}\times a/I_{z,a}$, $I_{z,a}$ and $I_{z,b}$ are the moments of inertia of the connecting beams and the span beams relative to the Z-axis, respectively. Substituting the parameters of folded beams listed in Table 1 into (1)-(3) yields $k_{/\!/}$= 2.73 N/m, $k_{\perp}$= 1.40 N/m, k_m= 8.84 N/m.

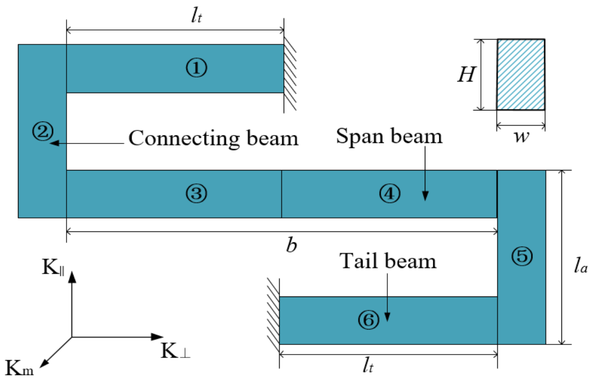

Figure 2: Serpentine beam with two folded segments.

As shown in Figure 1, the movable structure of the accelerometer is supported on the upper surface of the silicon substrate by eight serpentine springs. The equivalent stiffness along the orthogonal X, Y, and Z directions is K_x=K_y=4($k_{\perp}$+ $k_{/\!/}$) =16.52 N/m. K_z=8k_m=70.72 N/m.

3.2 The Resonance Frequency of the Accelerometer

Resonant frequency is a critical dynamic performance parameter of MEMS accelerometers. This parameter directly determines the device's operating bandwidth and dynamic response characteristics. For a spring-mass system, the natural resonant frequency is fundamentally determined by the structural stiffness and mass. The resonant frequency of the accelerometer is expressed by the following equation [28]:

$$f_i = \frac{1}{2\pi}\sqrt{\frac{K_i}{m}} \tag{4}$$

Where K_i denotes the spring constant of the serpentine spring beam in different directions. m denotes the mass of movable structure. The calculated resonant frequencies of the accelerometer are 743.95 Hz for the X- and Y-axes, and 1554.02 Hz for the Z-axis.

3.3 The Brownian Noise Density of the Accelerometer

Brownian noise (also known as thermal-mechanical noise) is the fundamental noise floor of accelerometers. It arises from the random thermal motion of air molecules impinging on the proof mass, and represents the theoretical lower limit of the accelerometer's detection resolution. The Brownian noise density of the accelerometer is expressed by the following equation [24]:

$$Noise_i = \frac{1}{9.8} \times \sqrt{\frac{8\pi k_B T f_i}{Qm}} \tag{5}$$

Where k_B (1.380649×10^{-23} *J/K)* is the Boltzmann constant, T is the ambient temperature (taken as 300 K at room temperature), $f_i$is the resonant frequency of each axis calculated from Equation (4), and Q is the mechanical quality factor. The calculated Brownian noise densities of the accelerometer are 1.37 $\mu g/\sqrt{Hz}$ for the X- and Y-axes, and 1.82 $\mu g/\sqrt{Hz}$ for the Z-axis. If the accelerometer is operated in vacuum, gas damping is strongly reduced and the mechanical quality factor Qincreases; according to Equation (5), the Brownian acceleration-noise density therefore decreases. Nevertheless, intrinsic structural and anchor losses still give rise to mechanical dissipation.

4 The Sensitivity of the Accelerometer

4.1 The Detection Sensitivity of In-Plane Acceleration

The in-plane acceleration is detected by equal-height comb capacitors with unequal gaps around the four sides of the proof mass. The comb capacitors at the top and bottom sides of the proof mass are shown in Figure 3 (a) and (b), respectively.

The capacitances of two sets of comb electrodes with initial gaps d_1 and d_2 are denoted as C_{d1i} and C_{d2i}, respectively, where i=1, 2…,48. The initial capacitances C_{x10} and C_{x20} of the 48 parallel-connected comb-electrode pairs located at the top and bottom sides of the proof mass are identical. Therefore, the total initial capacitance of the comb capacitors on the top and bottom sides of the proof mass can be derived using the following equation.

$$C_{x0} = C_{x10} + C_{x20} = 2 \times \sum_{i=1}^{24}(C_{d1i} + C_{d2i}) = 48\varepsilon A\left(\frac{1}{d_1} + \frac{1}{d_2}\right) \tag{6}$$

Where ε denotes the relative permittivity of the dielectric medium, and A is the overlapping area between the facing comb fingers.

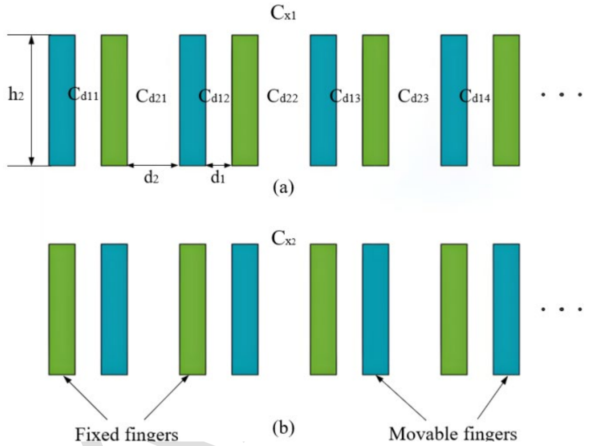

Figure 3: In-plane acceleration sensing comb capacitors. (a) Top capacitors; (b) Bottom capacitors.

The initial gap d_1 of the comb fingers at the top side of the proof mass decreases by Δd, while the initial gap d_2 of the comb fingers at the bottom side increases by Δd if subjected to X-axis acceleration along the negative direction. Therefore, the total change of capacitance is

$$\Delta C_x = \Delta C_{x1} + \Delta C_{x2} = 24\varepsilon A\begin{pmatrix} \frac{1}{d_1-\Delta d} + \frac{1}{d_2+\Delta d} \\ -\frac{1}{d_1+\Delta d} - \frac{1}{d_2-\Delta d} \end{pmatrix} \tag{7}$$

Since $\Delta d/d_1 \ll 1$, $\Delta d/d_2 \ll 1$ and $d_2 = 4d_1$, the relative change (γ_{xx}) of capacitance of capacitors used for detecting X-axis acceleration is given by the following equation.

$$\Delta\gamma_{XX} = \frac{\Delta C_x}{C_{x0}} \times 100\% = \frac{3}{4} \cdot \frac{\Delta d}{d_1} \times 100\% \tag{8}$$

Finite-element simulations were performed for all movable microstructures using the commercial software ANSYS Workbench. To ensure the reliability of finite element results, a mesh sensitivity analysis was carried out for the model. Four graded mesh levels were established, and the convergence was evaluated by the X-axis displacement and relative deviation. The detailed data are listed in Table 2. With the 2% relative difference as the convergence threshold [29], the fine mesh yields sufficiently convergent results and is thus selected for all simulations.

The displacement contour plot of the movable structure under 2g X-axis acceleration from finite element simulation is shown in Figure 4. The displacement of the movable comb fingers along X-axis is 0.95 µm. And the relative change (γ_{xx}) of capacitance is calculated to be 15.83% by (9). Thus, the ratio of γ_{xx} to the input X-axis acceleration is 7.92%/g.

Table 2: The analysis results of mesh sensitivity.

Mesh level	Number of nodes	X-axis displacement (μm)	Relative change
Coarse	108561	0.8883	—
Medium	243164	0.9362	5.39%
Fine	347980	0.9498	1.45%
Ultra-fine	449810	0.9512	0.15%

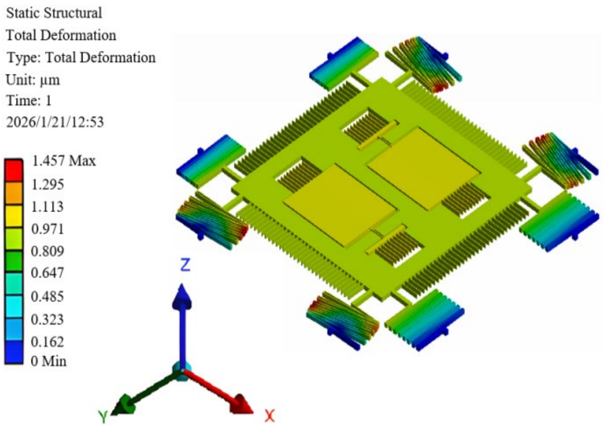

Figure 4: Displacement contour plot of the movable structure under 2g X-axis acceleration.

The theoretical X-axis displacement under 2 g acceleration is calculated as 0.91 μm based on the equivalent stiffness. This result yields a small relative error of 4.39% compared with the finite element simulation result of 0.95 μm, verifying the correctness of the accelerometer's triaxial stiffness coefficients. The structure and detection principle of comb capacitors used for detecting Y-axis acceleration are basically the same as those used for detecting X-axis acceleration. Similarly, applying a Y-axis acceleration of 2*g* in simulation produces a 0.95 μm displacement of the movable comb fingers. The relative change (γ_{yy}) of capacitance is calculated to be 15.83%. Thus, the ratio of γ_{yy} to the input Y-axis acceleration is calculated to be 7.92%/*g*.

4.2 The Detection Sensitivity of Out-of-Plane Acceleration

Two staggered seesaws located within the proof mass are used as sensitive elements to detect Z-axis acceleration. Comb capacitors with unequal height are arranged on both sides of each seesaw. Figure 5(a) and (b) depict the comb capacitors with unequal height on the upper and lower seesaws. The height of the movable fingers on the left side is consistent with the thickness of the proof mass and the height of the fixed fingers is half of the thickness of the proof mass. The relationship of height between the fingers on the right side is just the opposite.

Figure 6 (a) shows the motion of the upper seesaw under positive Z-axis acceleration. The movable fingers on the left side of the seesaw move along the positive Z-axis, thereby reducing the overlapping area and resulting in a reduction of capacitance C_{z1} by ΔC_{z1}. Similarly, the movable fingers on the right side move along the negative Z-axis, thereby reducing the overlapping area and resulting in a reduction of capacitance C_{z2} by ΔC_{z2}. Figure 6 (b) illustrates the motion of the lower seesaw under positive Z-axis acceleration. The movable fingers on the left side of

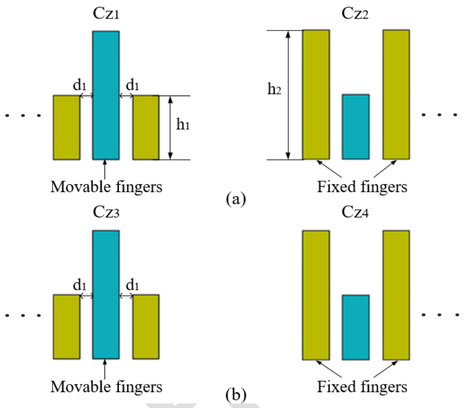

Figure 5: Capacitors of the two staggered seesaws. (a) Comb capacitors of upper seesaw; (b) Comb capacitors of lower seesaw.

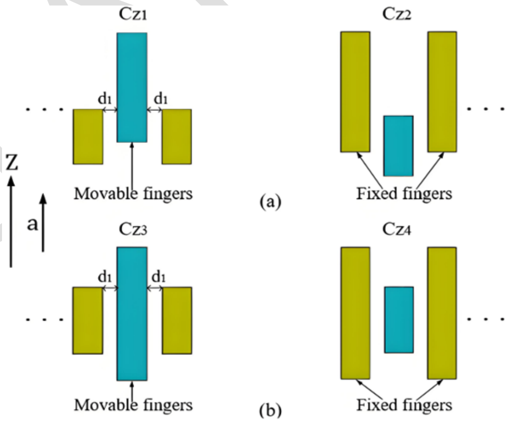

Figure 6: Overlapping state of unequal height capacitors under positive Z-axis acceleration.

the seesaw translate along the negative Z-axis, maintaining a constant overlapping area so that the capacitance C_{z3} remains unchanged. Similarly, the movable fingers on the right side move along the positive Z-axis, maintaining a constant overlapping area so that the capacitance C_{z4} remains unchanged. Conversely, the capacitance variation under negative Z-axis acceleration (Figure 7) is exactly opposite to that under positive Z-axis acceleration (Figure 6). Specifically, the upper seesaw exhibits no capacitance variation. The lower seesaw shows capacitance reductions of ΔC_{z3} and ΔC_{z4} for C_{z3} and C_{z4} respectively. Table 3 summarizes the capacitance variation trends of the four capacitors under positive and negative accelerations.

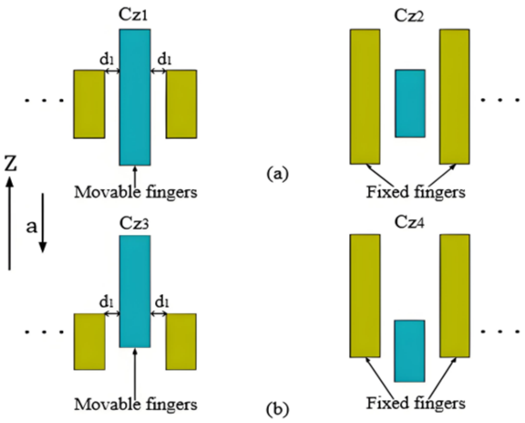

Figure 7: Overlapping state of unequal height capacitors under negative Z-axis acceleration.

Table 3: The changing trend of the capacitance of the four capacitors under ±z acceleration.

Direction of Z-axis acceleration	C_{z1}	C_{z2}	C_{z3}	C_{z4}
Positive	↓	↓	—	—
Negative	—	—	↓	↓

Taking the seesaw at the upper part of the proof mass as an example, the detection sensitivity of Z-axis acceleration is quantitatively analysed as follows. Figure 8 shows the torsional motion of the seesaw under positive Z-axis acceleration. Here, θ de notes the deflection angle of the seesaw around thetorsion beam. L_{right} and L_{left} denote the lengths of the right and left parts of the seesaw. l_{sz} is the length of comb fingers. The arc lengths swept out are$S_s = (L_{right} + l_{sz}) \cdot \theta$ for the right end of the right movable fingers and $s_q = L_{right} \cdot \theta$ for the right end of the proof mass.

The change in overlapping area between the right-side movable comb fingers and the fixed comb fingers under positive Z-axis acceleration is equal to the difference in area between two sectors of radii L_{right} and $L_{right}+l_{sz}$ subtending the same central angle θ. The resulting change of capacitance can be expressed as follows.

$$\Delta C_{right} = (\varepsilon \cdot \Delta A_{right})/d = \varepsilon \cdot \{5[(L_{right} + l_{sz})^2 - L_{right}^2] \cdot \theta\}/d \quad (9)$$

Where ΔA_{right} is the change of the overlapping area between the movable comb fingers and the fixed comb fingers on the right side of the seesaw under Z-axis positive acceleration.

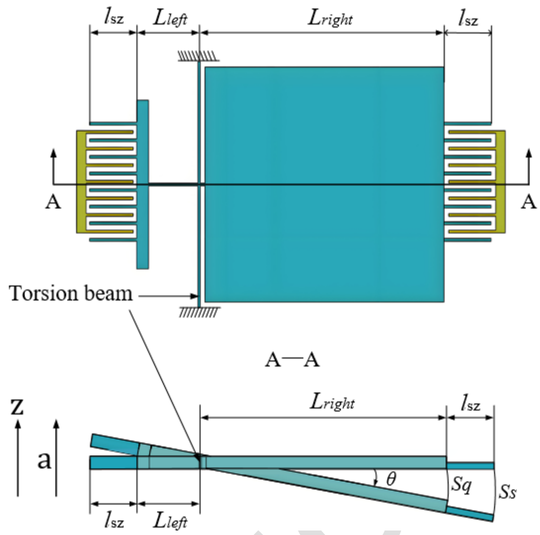

Figure 8: The torsional motion of the seesaw under Z-axis positive acceleration.

Similarly, the change of capacitance caused by the twisting motion of the left side of the seesaw at the upper part of the proof mass under Z-axis positive acceleration is

$$\Delta C_{left} = \varepsilon \cdot \{5[(L_{left} + l_{sz})^2 - L_{left}^2] \cdot \theta\}/d \quad (10)$$

This leads to an increase of ΔS_Z in the overlapping area between the movable and fixed comb fingers on the left side of the seesaw and a decrease of ΔS_Z on the right side. These two changes cancel each other. Thus, only the capacitance variation caused by the torsional displacement of the seesaw needs to be considered in the mechanism analysis. As mentioned previously, only one of the two seesaw sensing units in the unequal-height comb capacitor structure exhibits an effective capacitance change under Z-axis acceleration, while the other remains constant. Accordingly, the expression for the relative capacitance change rate (γ_{zz}) is

$$\gamma_{zz} = \frac{5\varepsilon\theta \cdot \{[(L_{right}+l_{sz})^2 - L_{right}^2] + [(L_{left}+l_{sz})^2 - L_{left}^2]\} \times 100\%}{(C_{Z1}+C_{Z2})d} \quad (11)$$

Figure 9 shows the displacement contour plot of the movable structure under a 2 g Z-axis acceleration from simulation analysis. The maximum deflection of the movable fingers on the heavier side of the seesaws relative to the static state is 2.44 μm, corresponding to a rotation angle of $\theta = 2.75\times10^{-3}$ rad. By substituting it into (11), the relative change (γ_{zz}) of capacitance is calculated to be 9.0%. The ratio of γ_{zz} to the input Z-axis acceleration is calculated to be 4.5%/g.

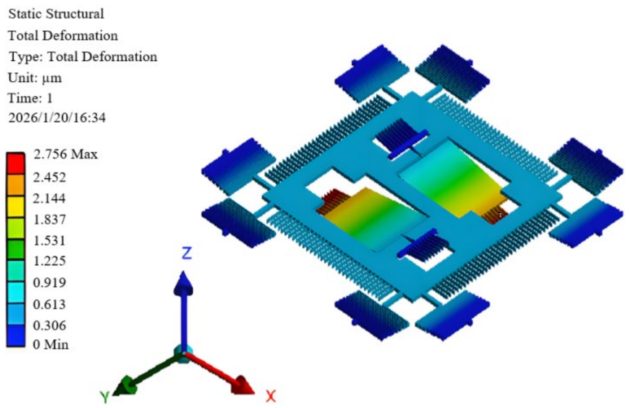

Figure 9: Displacement contour plot of the movable structure under 2g Z-axis acceleration.

In order to detect the magnitude and direction of acceleration, the four comb capacitors can be connected to form a Wheatstone bridge as shown in Figure 10. The output voltage generated is given by the following equation.

$$u_0 = \left(\frac{1}{1+C_{z3}/C_{z1}} - \frac{1}{1+C_{z2}/C_{z4}}\right) U_m \sin \omega t \qquad (12)$$

As the capacitances of C_{z1} and C_{z2} decrease under positive Z-axis acceleration while those of C_{z3} and C_{z4} remain unchanged, (12) indicates that the output voltage u_0 diminishes with increasing positive Z-axis acceleration. Conversely, the capacitances of C_{z1} and C_{z2} stay constant while those of C_{z3} and C_{z4} decrease under negative Z-axis acceleration; consequently, (12) shows that the output voltage u_0 rises with increasing negative Z-axis acceleration.

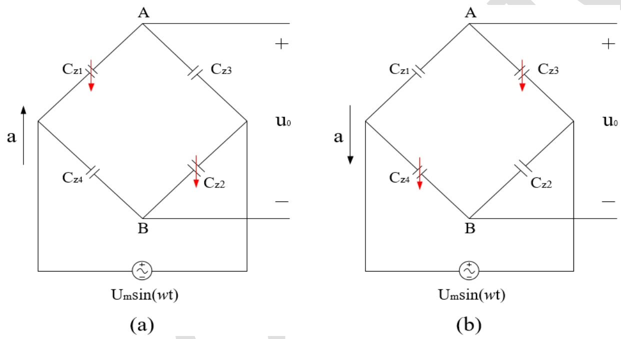

Figure 10: Displacement contour plot of the movable structure under 2g Z-axis acceleration.

4.3 *The Nonlinearity of the Accelerometer*

The nonlinearity of the proposed triaxial capacitive accelerometer mainly stems from the geometric nonlinearity of the serpentine-flexure supporting structures. When the proof mass deflects under applied acceleration, the serpentine flexures undergo slight geometric deformation, with axial-stress components developing within the beams. These stresses introduce high-order terms into the structural stiffness and cause a small deviation from the ideal linear displacement response. The nonlinearity was characterized via quasi-static simulation over the operational range of ±2 g, with the large-deformation formulation activated to reproduce the actual mechanical behavior.

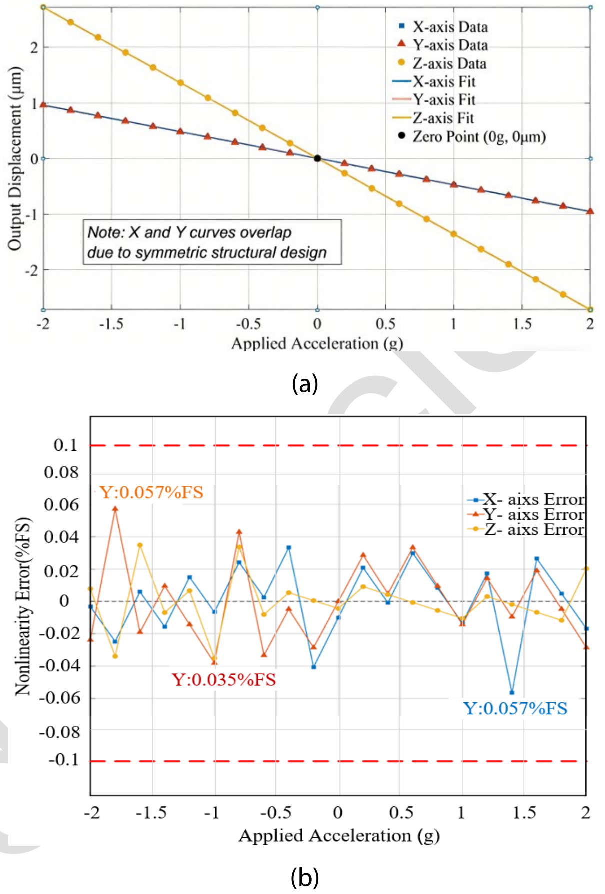

Figure 11: Scale factor linearity characterization of the triaxial accelerometer. (a) Output displacement response versus applied acceleration. The solid lines represent linear least-squares fits; (b) Nonlinearity error expressed as percentage of full-scale output.

Figure 11(a) depicts the simulated displacement responses of the movable comb fingers as a function of applied acceleration along all three axes, where the solid lines represent the linear least-squares fitting curves. Figure 11(b) quantifies the nonlinearity error expressed as a percentage of the full-scale output. The nonlinearity of the accelerometer is exceptionally low: 0.054% FS for the X-axis, 0.057% FS for the Y-axis, and 0.044% FS for the Z-axis.

As shown in Figure 11, two significant features are evident. First, the near overlap of X- and Y-axis responses in Figure 11(a) confirms the successful implementation of the symmetric in-plane structural design. Second, although visually amplified by the fine scale of the plot, the nonlinearity errors are calculated to fall within a narrow range of ±0.057% FS, which is below the typical performance threshold of ±0.1% FS as marked by the reference lines in Figure 11(b).

5 *The Cross-Axis Sensitivity of the Accelerometer*

Cross-axis sensitivity is defined as the ratio of an accelerometer's output when subjected to a lateral (off-axis) acceleration to its output under an equal magnitude of acceleration along the primary sensing axis.

5.1 Cross-Axis Sensitivity of X-Axis Detection Capacitors to Y-Axis Acceleration

The cross-axis sensitivity (δ_{xy}) of the capacitors (C_{x1}, C_{x2}) used for detecting X-axis acceleration under Y-axis acceleration is [30].

$$\delta_{xy} = \frac{S_{xy}}{S_{xx}} \times 100\% = \frac{\Delta C_x}{a_y \cdot C_{x0} \cdot S_{xx}} \times 100\% = \frac{4}{3} \cdot \frac{d_1}{l_{sx}} \times 100\% \qquad (13)$$

Where S_{xx} is the ratio of relative change of capacitance of capacitors (C_{x1}, C_{x2}) to the input X-axis acceleration. S_{xy} is the ratio of relative change of capacitance of capacitors (C_{x1}, C_{x2}) to the input Y-axis acceleration. ΔC_x is the capacitance change of capacitors (C_{x1}, C_{x2}) under Y-axis acceleration.

Substituting d_1 = 4.5 µm and l_{sx} = 250 µm listed in Table 1 into (26) yields δ_{xy} = 2.40%. Similarly, the cross-axis sensitivity δ_{yx} of the capacitors (C_{y1}, C_{y2}) used for detecting Y-axis acceleration under X-axis acceleration is calculated to be 2.40%. The validity of the calculated cross-axis sensitivity can be verified by finite element simulation. Figure 12 shows the displacement contour plot of the movable structure under a 2g Y-axis acceleration.

The movable comb fingers of the capacitors (C_{x1}, C_{x2}) have a displacement of 0.95 µm along Y-axis, i.e., Δx_y = 0.95 µm. The cross-axis sensitivity (δ_{xy}) is calculated to be 2.41%, which agrees with the theoretical analysis. Similarly, simulation analysis confirms that the cross-axis sensitivity of the capacitors (C_{y1}, C_{y2}) used for detecting Y-axis acceleration under X-axis acceleration is δ_{yx} = 2.41%.

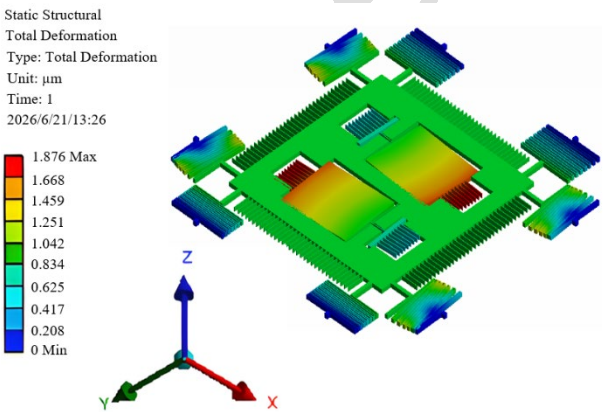

Figure 12: Displacement contour plot of the movable structure under 2g Y-axis acceleration.

5.2 Cross-Axis Sensitivity of Z-Axis Detection Capacitors to X-Axis Acceleration

In the proposed triaxial capacitive accelerometer, the seesaws used for detecting Z-axis acceleration feature different capacitance-variation behaviors under in-plane accelerations. Under X-axis acceleration, the overlapping area of the comb capacitors on both sides of the seesaws varies, whereas the gap between the comb capacitors changes under Y-axis acceleration.

As shown in Figure 13, the seesaw structure will move in the negative X-axis direction under the action of positive X-axis acceleration. At this time, the overlap area between the movable comb fingers on the left side of the seesaw and the fixed comb fingers on their upper and lower sides increases by ΔS_1, resulting in an increase of ΔC_{zx1} in capacitance C_{z1}. Conversely, the overlap area between the movable comb fingers on the right side of the seesaw and the fixed comb fingers on their upper and lower sides decreases by ΔS_2, leading to a decrease of ΔC_{zx2} in capacitance C_{z2}.

Similarly, capacitance C_{z3} increases by ΔC_{zx3} and capacitance C_{z4} decreases by ΔC_{zx4} under positive X-axis acceleration. The following relationship holds:

$$f(x, y) = \sum_{i=0}^{N-1} c_i (x_i^2 + y_i^2) \qquad (14)$$

Since the four sets of capacitors (C_{z1}, C_{z2}, C_{z3}, C_{z4}) used for Z-axis acceleration detection have equal initial capacitances, all denoted as C_z, when an AC excitation voltage ($U_m sin\omega t$) is applied to the input terminals of the capacitive bridge, the corresponding output voltage u_0 expression (12) can be rewritten as:

$$u_0 = \left(\frac{1}{1+\frac{C_z+C_{zx1}}{C_z+C_{zx1}}}\right) - \left(\frac{1}{1+\frac{C_z-C_{zx1}}{C_z-C_{zx1}}}\right) U_m sin\omega t \approx 0 \qquad (15)$$

Therefore, the output voltage u_0 is almost independent of the X-axis acceleration, indicating that the cross-axis sensitivity δ_{zx} of the comb capacitors (C_{z1}, C_{z2}, C_{z3}, C_{z4}) for Z-axis acceleration detection in this capacitive accelerometer is close to zero under X-axis acceleration excitation.

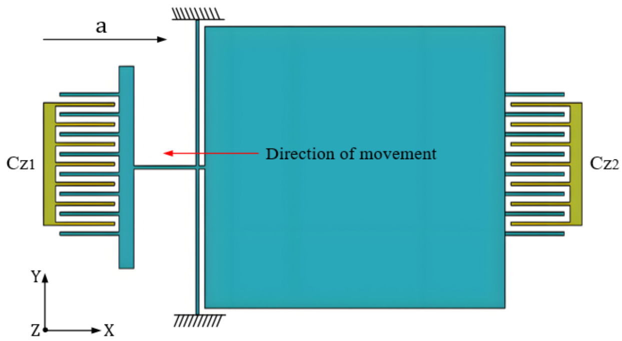

Figure 13: Motion of the upper seesaw under X-axis positive acceleration.

5.3 Cross-Axis Sensitivity of Z-Axis Detection Capacitors to Y-Axis Acceleration

The total capacitance of the left comb capacitors of the seesaw located in the upper part of the proof mass connected in parallel is C_{z1}. And the total capacitance of the right comb capacitors connected in parallel is C_{z2}. As shown in Figure 14, the gap between the movable fingers on the left side of the seesaw and the fixed fingers on the lower side increases by Δd_1 under Y-axis positive acceleration, resulting in a capacitance decrease of ΔC_{zy1}. The gap between the fixed fingers on its upper side decreases by Δd_2, resulting in a capacitance increase of ΔC_{zy2}.

Since $\Delta d_1 = \Delta d_2$, $\Delta C_{zy1} = \Delta C_{zy2}$. The total capacitance of the comb capacitors on the left side of the seesaw connected in parallel is

$$C_{z1}{}' = C_{z1} - \Delta C_{zy1} + \Delta C_{zy2} = C_{z1} \tag{16}$$

Similarly, it can be concluded that the total capacitance of the parallel-connected comb capacitors on the right side of the seesaw remains unchanged. Accordingly, the total capacitance of the comb capacitors on both sides of the seesaw remains constant under positive and negative Y-axis acceleration, implying that the cross-axis sensitivity δ_{zy} of the Z-axis acceleration detection capacitors C_{z1}~C_{z4} is nearly zero under Y-axis acceleration.

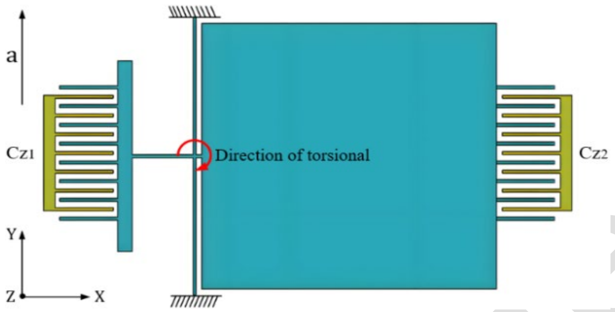

Figure 14: Torsional motion of the upper seesaw under Y-axis positive acceleration.

5.4 Cross-Axis Sensitivity of In-Plane Detection Capacitors to Z-Axis Acceleration

The cross-axis sensitivity (δ_{xz}) of the capacitors (C_{x1}, C_{x2}) used for detecting the X-axis acceleration under the Z-axis acceleration is

$$\delta_{xz} = \frac{S_{xz}}{S_{xx}} \times 100\% = \frac{\Delta x_z}{S_{xx} h_2} \times 100\% = \frac{4}{3} \cdot \frac{d_1}{h_2} \cdot \frac{K_x}{K_z} \times 100\% \tag{17}$$

The cross-axis sensitivity (δ_{yz}) of the capacitors (C_{y1}, C_{y2}) used for detecting the Y-axis acceleration under the Z-axis acceleration is

$$\delta_{yz} = \frac{S_{yz}}{S_{yy}} \times 100\% = \frac{\Delta y_z}{S_{yy} h_2} \times 100\% = \frac{4}{3} \cdot \frac{d_1}{h_2} \cdot \frac{K_y}{K_z} \times 100\% \tag{18}$$

Substituting d_1 and h_2 listed in Table 1 into (17) and (18) yields $\delta_{xz} = \delta_{yz}$ =2.80%.

Figure 15 shows the front-view displacement contour plot of the movable structure under a 2 g acceleration obtained by finite element simulation. The movable comb fingers of the capacitors (C_{x1}, C_{x2}, C_{y1} and C_{y2}) have a displacement of 0.22 μm along the Z-axis. The cross-axis sensitivities (δ_{xz}, δ_{yz}) are calculated to be 2.79 % by Eqs. (17) and (18). The results of these simulations are close to those of the theoretical analysis.

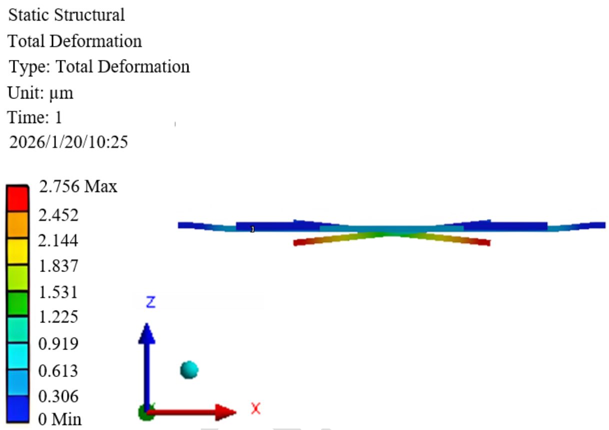

Figure 15: Displacement contour plot of the movable structure under 2g Z-axis acceleration.

6 Dynamic Analysis

6.1 Modal Analysis

Mode refers to the natural vibration characteristics of a mechanical structure. Each mode corresponds to a specific vibration frequency and vibration mode. The vibration modes and natural resonance frequencies of each mode of the triaxial capacitive accelerometers can be obtained through modal analysis, thereby understanding the response state of the accelerometer at different frequencies. Modal analysis was performed to determine the first six vibration modes of the accelerometer, as shown in Figure 16.

Table 4 lists the corresponding natural frequencies of each mode, where the 1st, 2nd, and 3rd modes represent translational vibrations along the Y-axis, X-axis, and Z-axis, respectively, while the 4th, 5th, and 6th modes correspond to rotational vibrations about the Z-axis, Y-axis, and X-axis, respectively. The natural frequencies of the Y-axis, X-axis, and Z-axis translational modes from simulation are 766.53 Hz, 774.17 Hz, and 1478.35 Hz, respectively. For comparison, the theoretical natural frequencies calculated using Equations (4) and (5) are 743.95 Hz for both X- and Y-axes and 1554.02 Hz for the Z-axis. The corresponding relative errors between theoretical and simulated results are 3.04% for the Y-axis, 4.06% for the X-axis, and 4.87% for the Z-axis. The good agreement between the theoretical and simulated results confirms the accuracy of the derived resonant frequency equations.

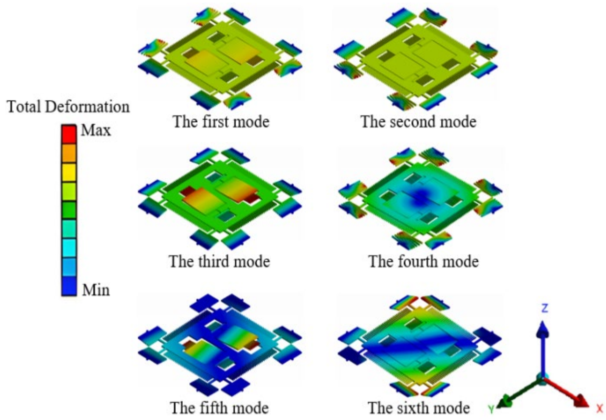

Figure 16: The first six mode shapes of the triaxial capacitive accelerometer.

Table 4: The first six modal frequencies of the accelerometer.

Order	Frequency /Hz
1	766.53
2	774.17
3	1478.35
4	1775.90
5	1811.30
6	2239.00

6.2 Harmonic Response Analysis

Based on the structural geometric parameters and gas film damping theory, the damping coefficient of the comb-drive accelerometer at standard atmospheric pressure conditions is mainly derived from squeeze-film damping and slide-flow damping. The calculation formulas for the damping coefficient are as follows [31]:

$$c_{slide} = \frac{\mu A}{d} \tag{19}$$

$$c_{squeeze} = \frac{12\mu L_c h^3}{d^3} \tag{20}$$

Where μ denotes the viscosity of air, A is the effective area of the electrodes, L_c is the electrode length, h is the electrode thickness and d is the gap of comb fingers. Therefore, the damping ratios corresponding to the X and Y axes are $\zeta_x = \zeta_y = 0.83$. The quality factors corresponding to the X and Y axes are $Q_x = Q_y = 1/2\zeta = 0.60$.

The damping ratio of the torsion proof mass is [32]

$$\zeta_z = \frac{\sqrt{12\mu \times p_a} \times {L_L}^2}{2\sqrt{mK_z}{g_0}^2} \times \sum_{i=1}^{\infty}\sum_{j=1}^{\infty}\left(\frac{16L_L L_W}{i^2 j^2 \pi^4}\right) \times \left\{L - \left[1 + (-1)^{i+1}\right]\left(\frac{L_L}{2} + l\right)\right\}^2 \times \frac{\left[(i\pi)^2 + \left(j\pi\frac{L_L}{L_W}\right)^2\right]}{\frac{12\mu\omega^2 {L_L}^4}{p_a g_0^2} + \left[(i\pi)^2 + \left(j\pi\frac{L_L}{L_W}\right)^2\right]^2} \tag{21}$$

Where p_a is the gas pressure, g_0 is the initial gap between the seesaw and substrate, ω is the angular frequency, i and j are summation integers (where i = 1, 2, 3… and j = 1, 3, 5…), L_L is the length of the seesaw, L_W is the width of the seesaw, l is the distance from the rotating shaft to the center of the seesaw.

Based on automatic control theory, the system yields optimal dynamic characteristics when the damping ratio is adjusted to 0.707. Under standard atmospheric pressure, calculations via Equation (21) demonstrate that the damping ratio of the Z-axis sensing unit reaches the optimal value of 0.707 at an initial gap of 12.20 μm and the quality factor is $Q_z = 1/2\zeta = 0.707$.

The harmonic response curves under 1 g acceleration are illustrated in Figure 17. The amplitude frequency responses of the accelerometer along all three axes show a smooth and monotonically decreasing trend. This is mainly attributed to the high structural damping ratio, which effectively suppresses the resonance risk under broadband excitation and avoids abrupt variations in amplitude.

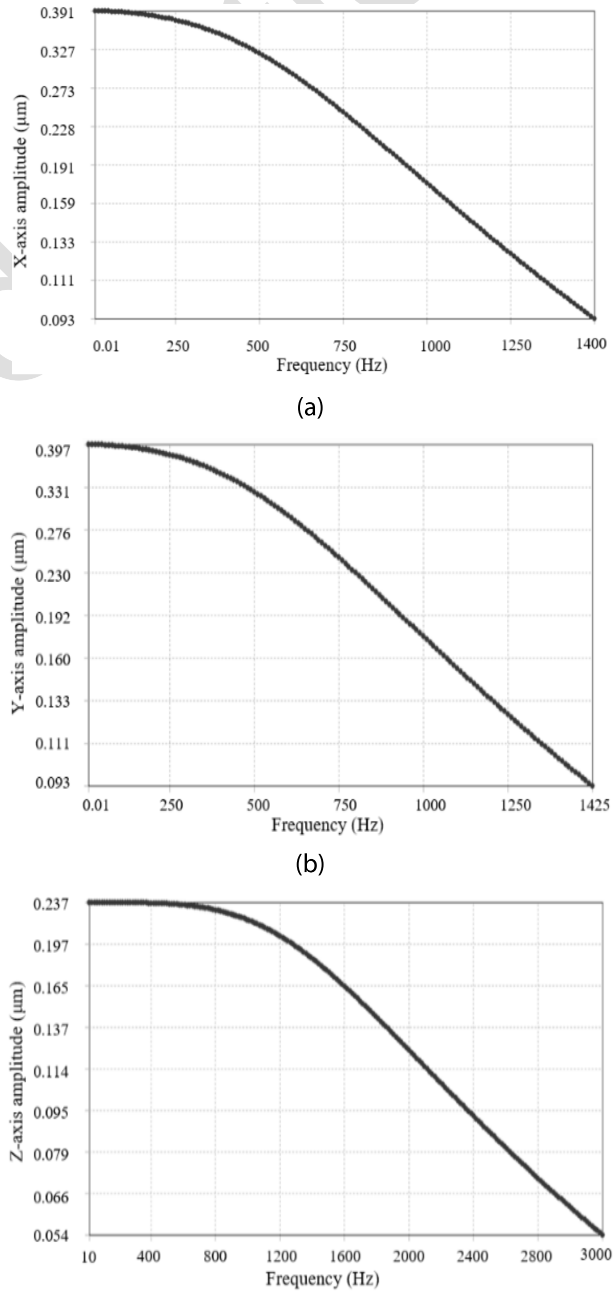

(c)

Figure 17: The curve of amplitude-frequency characteristic. (a) Frequency response under 1g X-axis acceleration; (b) Frequency response under 1g Y-axis acceleration; (c) Frequency response under 1g Z-axis acceleration.

7 Fabrication Process

To ensure the manufacturability of the proposed comb-type accelerometer while avoiding anchor failure caused by lateral undercut in conventional SOI processes, this chapter presents an optimized fabrication process based on SOG bonding. The core of this approach involves pre-etching release cavities into the glass substrate, which enables permanent anchoring of fixed structures through bonding, thereby fundamentally eliminating the aforementioned reliability issue. The main process flow is illustrated in Figure 18. And the specific process flow is as follows : (a) Preparation and cleaning of silicon wafer; (b) Fabrication of groove structures on glass substrate; (c) Anodic bonding of silicon and glass; (d) Thinning of silicon wafer to a thickness of 50 μm; (e) First-time photoresist coating; (f) First lithography for 25 μm structure patterning; (g) Second-time photoresist coating; (h) Second lithography for 25 μm structure patterning with release of movable structures.

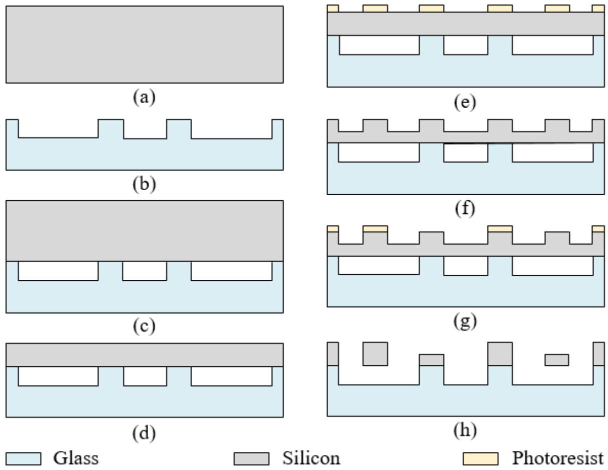

Figure 18: Process flow diagram.

8 Conclusion

This paper presents a novel triaxial accelerometer with two staggered seesaws embedded in a single proof mass, which is integrated with in-plane comb capacitors. The proposed staggered dual-seesaw design maintains good process compatibility with in-plane comb capacitors, and avoids the drawbacks of traditional sidewall capacitors for out-of-plane Z-axis acceleration sensing. The proposed design has a larger mass difference between the two sides of the torsion beam compared with the centrally symmetric dual-seesaw structure, which enables greater torsional displacement and more obvious capacitance variation under out-of-plane acceleration, thereby improving the Z-axis detection sensitivity. As shown in Table 5, the proposed accelerometer exhibits higher sensitivity while maintaining low cross-axis sensitivity and noise density compared with previously reported accelerometers [6], [17], [18], [21], [28]. Accordingly, this accelerometer has the potential to be applied in scenarios such as geological hazard detection, vibration monitoring, industrial automatic control, and structural health monitoring.

Table 5: Performance comparison between the proposed capacitive accelerometer and existing devices

Parameter	Range (g)	Full-scale capacitance change(X/Y) (%)	Full-scale capacitance change(Z) (%)	Cross-axis Sensitivity (%)	Noise densities (X/Y) (μg/√Hz)	Noise densities (Z) (μg/√Hz)
F. Chen [6]	±4	6.35	1.74	3	18.04	10.96
Y. W. Hsu [17]	±2	2.98	5.98	4	140	49
J. Xie [18]	±3	15.85	2.02	3	3.02	2.18
C. Y. Yeh [21]	±6	2.64	0.90	5	350	1500
Pazhooh [33]	±10	13.75	9.31	1	7.5	10.8
This paper	±2	15.83	9.00	3	1.37	1.82

9 Acknowledgments

Financial support for this work was provided by the National Natural Science Foundation of China under Grant No. 62334006. Partial funding was also received from the Zhejiang Natural Science Foundation (Grant No. LZ22F040002) and the Open Project of the State Key Laboratory of Sensor Technology (Grant No. SKT2305).

10 References

[1] C. Wang, F. Chen, Y. Wang, et al., "Micromachined Accelerometers With Sub-μg/√ Hz Noise Floor: A Review," Sensors, vol. 20, no. 14, pp. 4054, 2020, https://doi.org/10.3390/s20144054.

[2] S. Tez, U. Aykutlu, M. M. Torunbalci, et al., "A Bulk-Micromachined Three-Axis Capacitive MEMS Accelerometer on a Single Die," Journal of Microelectromechanical Systems, vol. 24, no. 5, pp. 1264–1274, 2015,https://doi.org/10.1109/JMEMS.2015.2451079.

[3] R. Li, Z. Mohammed, M. Rasras, et al., "Design, Modelling and Characterization of Comb Drive MEMS Gap-Changeable Differential Capacitive Accelerometer," Measurement, vol. 169, pp. 108377, 2021, https://doi.org/10.1016/j.measurement.2020.108377.

[4] A. Sthuthi, G. Nithya, K. N. Kumar, et al., "Design and Simulation of Dual-Axis MEMS Accelerometer," Materials Today: Proceedings, 2023, 10.1016/j.matpr.2023.05.569.

[5] S. Kavitha, R. J. Daniel, K. Sumangala, "Design and Analysis of MEMS Comb Drive Capacitive Accelerometer for SHM and Seismic Applications," *Measurement*, vol. 93, pp. 327–339, 2016, 10.1016/j.measurement.2016.07.029.

[6] F. Chen, Y. Zhao, J. Wang, et al., "A Single-Side Fabricated Triaxis (111)-Silicon Microaccelerometer With Electromechanical Sigma–Delta Modulation," *IEEE Sensors Journal*, vol. 18, no. 5, pp. 1859–1869, 2017, 10.1109/JSEN.2017.2785394.

[7] M. K. Dounkal, R. K. Bhan, N. Kumar, "A New Improved Vertical Comb Type Differential Capacitive Sensing Micro Accelerometer Using Silicon-on-Insulator Wafer Technology," *Journal of Micromechanics and Microengineering*, vol. 30, no. 10, pp. 105008, 2020, 10.1088/1361-6439/ab9b13.

[8] P. Martha, N. Kadayinti, V. Seena, "A CMOS-MEMS Accelerometer With U-Channel Suspended Gate SOI FET," *IEEE Sensors Journal*, vol. 21, no. 9, pp. 10465–10472, 2021, 10.1109/JSEN.2021.3060186.

[9] M. Taj, G. Vikram, "Design and Simulations of High-Sensitivity Multi-Directional Inertial Sensor," *IEEE Sensors Journal*, vol. 22, no. 1, pp. 190–194, 2021, 10.1109/JSEN.2021.3126469.

[10] G. Dai, M. Li, X. He, et al., "Thermal Drift Analysis Using a Multiphysics Model of Bulk Silicon MEMS Capacitive Accelerometer," *Sensors and Actuators A: Physical*, vol. 172, no. 2, pp. 369–378, 2011, 10.1016/j.sna.2011.09.016.

[11] J. Li, R. Feng, X. Wang, et al., "A Micromachined Silicon-on-Glass Accelerometer With an Optimized Comb Finger Gap Arrangement," *Micromachines*, vol. 15, pp. 1173, 2024, 10.3390/mi15091173.

[12] M. H. Tsai, Y. C. Liu, C. M. Sun, et al., "A CMOS-MEMS Accelerometer With Tri-Axis Sensing Electrodes Arrays," *Procedia Engineering*, vol. 5, pp. 1083–1086, 2010, 10.1016/j.proeng.2010.09.298.

[13] Y. Yin, B. Sun, F. Han, "Self-Locking Avoidance and Stiffness Compensation of a Three-Axis Micromachined Electrostatically Suspended Accelerometer," *Sensors*, vol. 16, no. 5, pp. 711, 2016, 10.3390/s16050711.

[14] S. Tez, U. Aykutlu, M. M. Torunbalci, et al., "A Bulk-Micromachined Three-Axis Capacitive MEMS Accelerometer on a Single Die," *Journal of Microelectromechanical Systems*, vol. 24, no. 5, pp. 1264–1274, 2015, 10.1109/JMEMS.2015.2451079.

[15] F. Chen, Y. Zhao, H. Zou, et al., "A Front-Side Non-SOI Fabricated Tri-Axis Capacitive Accelerometer With Electromechanical Sigma-Delta Modulators Interface," in *2017 19th International Conference on Solid-State Sensors, Actuators and Microsystems (TRANSDUCERS)*, 2017, pp. 930–933, 10.1109/TRANSDUCERS.2017.7994202.

[16] Y. W. Hsu, S. T. Lin, C. S. Lin, et al., "A Low-G Three-Axis Accelerometer IC," in *2009 4th International Microsystems, Packaging, Assembly and Circuits Technology Conference*, 2009, pp. 319–322, 10.1109/impact.2009.5382181.

[17] Y. W. Hsu, H. T. Chien, C. S. Lin, et al., "A Capacitive Low-G Three-Axis Accelerometer," in *2008 International Conference on Electronic Materials and Packaging*, 2008, pp. 325–328, 10.1109/EMAP.2008.4784294.

[18] J. Xie, R. Agarwal, Y. Liu, et al., "A Three-Axis SOI Accelerometer Sensing With Both In-Plane and Vertical Comb Electrodes," *Microsystem Technologies*, vol. 18, no. 3, pp. 325–332, 2012, 10.1007/s00542-011-1393-9.

[19] H. Hamaguchi, K. Sugano, T. Tsuchiya, et al., "A Differential Capacitive Three-Axis SOI Accelerometer Using Vertical Comb Electrodes," in *TRANSDUCERS 2007 - 2007 International Solid-State Sensors, Actuators and Microsystems Conference*, 2007, pp. c, 10.1109/SENSOR.2007.4300425.

[20] A. Sadat, H. Qu, C. Yu, et al., "Low-Power CMOS Wireless MEMS Motion Sensor for Physiological Activity Monitoring," *IEEE Transactions on Circuits and Systems I: Regular Papers*, vol. 52, no. 12, pp. 2539–2551, 2005, 10.1109/TCSI.2005.857772.

[21] C. Y. Yeh, J. T. Huang, S. H. Tseng, et al., "A Low-Power Monolithic Three-Axis Accelerometer With Automatically Sensor Offset Compensated and Interface Circuit," *Microelectronics Journal*, vol. 86, pp. 150–160, 2019, 10.1016/j.mejo.2019.03.005.

[22] M. Haris, H. Qu, "Fully Differential CMOS-MEMS Z-Axis Accelerometer With Torsional Structures and Planar Comb Fingers," *Journal of Micro/Nanolithography, MEMS and MOEMS*, vol. 9, no. 1, pp. 013031-1–013031-7, 2010, 10.1117/1.3295714.

[23] H. Qu, D. Fang, H. Xie, "Mirofabrication and Characterization of an Integrated 3-Axis CMOS-MEMS Accelerometer," in *2007 NSTI Nanotechnology Conference and Trade Show - NSTI Nanotech 2007*, 2007, pp. 13–16.

[24] H. Qu, D. Fang, H. Xie, "A Monolithic CMOS-MEMS 3-Axis Accelerometer With a Low-Noise, Low-Power Dual-Chopper Amplifier," *IEEE Sensors Journal*, vol. 8, no. 9, pp. 1511–1518, 2008, 10.1109/JSEN.2008.923582.

[25] S. H. Tseng, C. Y. Yeh, A. Y. Chang, et al., "A Monolithic Three-Axis Accelerometer With Wafer-Level Package by CMOS MEMS Process," in *Proceedings*, 2017, vol. 1, no. 4, pp. 337, 10.3390/proceedings1040337.

[26] H. Qu, H. Xie, "Process Development for CMOS-MEMS Sensors With Robust Electrically Isolated Bulk Silicon Microstructures," *Journal of Microelectromechanical Systems*, vol. 16, no. 5, pp. 1152–1161, 2007, 10.1109/JMEMS.2007.906079.

[27] G. K. Fedder, "Simulation of Microelectromechanical Systems," Ph.D. dissertation, Univ. California, Berkeley, CA, USA, 1994, 10.2308/jis.2000.14.2.151.

[28] S. Y. Gao, H. M. Shen, *Vibration Mechanics*, 2nd ed. Beijing: Higher Education Press, 2011.

[29] L. Kwaśniewski, "Application of Grid Convergence Index in FE Computation," *Bulletin of the Polish Academy of Sciences: Technical Sciences*, no. 1, 2013, 10.2478/bpasts-2013-0010.

[30] J. Han, Y. Zhu, G. Tao, et al., "A Triaxial Accelerometer Based on Differential Resonant Beams and Force-Balanced Capacitive Plates," *IEEE Sensors Journal*, vol. 19, no. 16, 2019, 10.1109/JSEN.2019.2911740.

[31] S. Ghasemi, B. Sotoudeh, M. Pazhooh, "Design and Simulation of a Novel MEMS-Based Single Proof Mass Three Axis Piezo Capacitive Accelerometer," *Microsystem Technologies*, vol. 30, no. 3, pp. 279–289, 2024, 10.1007/s00542-023-05604-9.

[32] Z. H. Qi, Z. Y. Zhang, "Analysis on Dynamic Performance of Torsional MEMS Capacitive Accelerometer," *Microprocessors*, vol. 44, no. 4, pp. 33–37, 2021, 10.3969/j.issn.1002-2279.2021.04.009.

[33] M. Pazhooh, S. Ghasemi, "Design and Simulation of a MEMS Decoupled Single Proof Mass Three-Axis Capacitive Accelerometer With Ultra-Low Cross-Axis Error," *Microsystem Technologies*, vol. 31, no. 10, pp. 2983–2996, 2025, 10.1007/s00542-025-05926-w.

Arrived: 25.06.2025
Accepted: 14.09.2026